Journal of Marine Science and Technology (2018) 23:899–914
https://doi.org/10.1007/s00773-017-0519-x

ORIGINAL ARTICLE

Growth and coexistence of structural and lift force modes in vortex-induced vibration of a flexible riser

Yoshiki Nishi[1] · Munekazu Motoyoshi[1] · Tatsuyuki Ueda[1]

Received: 30 March 2017 / Accepted: 24 December 2017 / Published online: 12 January 2018

Abstract
This study addresses the vortex-induced vibration of a flexible riser pipe. The primary purpose is to determine the fluid–structure interaction mechanism for the modal growth of structural and lift force modes formed along the vibrating riser, and to obtain the fundamental relationship between lift force and elasticity. To this end, a linear theory representing the essence of the vibration mechanics is described, and the mechanical properties involved in the theory are examined by performing eigenvalue analysis. In this theory, the fluid–structure interaction is shown to be mainly governed by spatial correlations among a vertical profile of flow velocities and structural eigenmode functions. The presence of shear induces growth of one or more structural modes, depending on the strength of the shear, and energy necessary for the structural mode growth is supplied from different lift force modes as well as the same mode of lift force. The dominance of multiple frequency components can be explained by differences in growth rate among prominent growing modes.

Keywords Riser · VIV · Structural mode · Lift force mode

1 Introduction

Recent increases in depth at installation sites of production riser pipes require them to function in more severe ocean environments. Their task is to serve as paths for fossil fuels to be conveyed from the sea floor to platforms on the sea surface, and they have to be placed for long service periods, subjected to vibration caused by surrounding currents. The present trend of increasing riser length makes it difficult to predict how the vibration will occur along a riser pipe, and accordingly to know the extent of material fatigue accumulation in the pipe.

Mechanically, a production riser pipe can be considered to be a beam with both its extremities fixed. Structural mechanics theory shows that such a beam has vibratory motions with nodes and antinodes (modal configuration). Experiments have confirmed such vibrations in flexible models of risers (e.g., [1–3]). Particularly, recent advances in experimental methods captured a clear image of the fluid at a wake interfering with a moving flexible structure (e.g., [4–7]), and enabled the measurements of both the cross flow and inline components of displacements and forces along a flexible cylinder (e.g. [8]). These efforts have revealed how the viscous fluid dynamics is related to the modal configuration and its associated vibratory frequency. It is important to be able to specify the modal configuration which dominates the vibration, because it is closely related to the stress in the riser [9].

The industrial demand has led engineers and researchers to attempt to understand the vibration of long slender structures subjected to fluid flow. A few achievements produced by these efforts are simulation tools [10–13]. These include databases for estimating hydrodynamic forces, which have been constructed by collecting measurement results of the forces acting on experimental models in test tanks, making it possible to conduct a practical and realistic simulation. As an example of simulation methods without such a database, there is one which uses computational fluid dynamics (CFD) applied to the entire length of a riser, e.g., [14–17]. These works successfully captured the complicated patterns of vortex generation and shedding in two- or three-dimensional numerical simulations.

The fact remains that a little clear understanding has thus far been achieved regarding fluid–structure interaction occurring in a riser undergoing vortex-induced vibration

✉ Yoshiki Nishi
nishi-yoshiki-rg@ynu.ac.jp

[1] Department of Systems-Design for Ocean-Space, Yokohama National University, Yokohama, Japan

(VIV). In particular, we have not sufficiently determined how vortex-induced forces interact with a vibrating flexible body. This study examines the interaction in detail, and reveals the mechanism underlying the relationship between the lift force and elasticity of a long slender structure.

The complexity of the VIV of the riser stems primarily from spatial nonuniformity in the vertical profile of fluid flow around the riser. Certain oceanographic observations found that there are flow velocity shears at locations where risers were installed [18]. This has also led many researchers to address the motion of flexible slender structures under a shear flow, e.g., [2, 19–21], providing some suggestive insight on the relationship of the modal growth to the shear. To the end mentioned above, this study attempts to conduct a mathematical analysis based on a linear theory. VIV is one of the vibrations with a limit cycle, and thus has a nonlinear property. We infer that risers installed in the actual ocean experience both matured and unmatured states of VIV. The unmatured state means that the VIV is in the course of growing and has a small amplitude. In the matured state, the VIV has the maximal amplitude under a flow speed condition, in which the oscillation of wake can be regarded as the limit cycle. An examination of the unmatured state as well as the matured state has an academic value, because the fluid–structure interaction along a flexible riser has been not yet sufficiently revealed. When focusing on the initial growing state of VIV, within which the amplitude is not so large, the linear analysis is applicable. If the linear analysis produces a solution for the issue posed above, it can lay a mechanical foundation, based on which mechanically adequate simulations can be performed. To make the foundation more firm, there is still room for linear analysis of the interaction between the lift force and elastic body.

Analytical approaches, e.g., [21–24], have been employed to investigate the modal configuration of a riser. Eigenmode functions, which are the most important when discussing the modal configuration of a vibrating riser, were computed using certain methods, e.g., [25–27]. Referring to those studies, we calculated the eigenmode functions to build our analytical method.

Expecting that the wake oscillator model is applicable to the interaction between the lift force and elasticity, this study applied it to compute the lift force. The basis of this model is the simplification of the oscillatory rotational motion of the wake region behind a moving body into the rotation of a rigid bar. Although this simplification is made under certain approximations, it involves the essence of hydrodynamics and vibration mechanics for the VIV. Some studies used the model for simulating time variations in long slender structures [28, 29]. The simplified form of the model is well suited to the mathematical approach.

This study attempts to theoretically determine the fluid–structure interaction involved in the VIV of the riser using the eigenmode function and wake oscillator model mentioned above. To this end, a matrix expressing explicitly the fluid–structure interaction is introduced.

Table 1 Independent and dependent variables

Symbol	Definition	Unit
t	Time	s
s	Lagrangian coordinate along pipe	m or –
C_L	Lift coefficient	–
y	Transverse displacement at a point on pipe	m
Y	Dimensionless transverse displacement at a point on pipe	–

"–" means dimensionless

Table 2 Parameter list

Symbol	Definition	Value	Unit
a^*	Dimensionless equivalent length	0.75	–
C_D	Drag coefficient	1.00	–
d	Outer diameter of pipe	0.40	m
E	Young's modulus	2.10×10^{11}	N m^{-2}
E^*	Dimensionless bending stiffness	2.62×10^{-7}	–
f	Slope of lift curve	1.16	rad^{-1}
g	Gravity acceleration	9.80	m s^{-2}
I	Moment of inertia of pipe area	5.20×10^{-4}	m^4
l	Half-length of wake	$1.10d$	m
L	Entire length of riser	5.00×10^3	m
M	Pipe mass per unit length	339.70	kg m^{-1}
N	Number of mode expansion	50	
q	Breadth of wake	$1.25d$	m
P'	Nonlinear damping coefficient	33.64	–
T	Tension		N
V	Fluid velocity		m s^{-1}
α	Dimensionless tension		–
ξ	Self-excitation coefficient	3.80×10^{-2}	
ρ	Sea water density	1.00×10^3	kg m^{-3}
ω_v	Vortex shedding frequency		rad s^{-1}
ω_v^*	Dimensionless vortex shedding frequency		–

"–" means dimensionless

2 Analytical method

The mathematical symbols representing the relevant variables are listed in Table 1.

The parameters used to build the theory are defined in Table 2, with the exception of certain parameters defined in the text. The coordinate s specifies a length at a point on the pipe measured from the bottom extremity.

2.1 Governing equations and energy equation

The displacement transverse to the flow direction is governed by the following equation of motion for an Euler–Bernoulli beam excited by hydrodynamic forces:

$$M\frac{\partial^2 y}{\partial t^2} - \frac{\partial}{\partial s}\left(T\frac{\partial y}{\partial s}\right) + EI\frac{\partial^4 y}{\partial t^4} = \frac{1}{2}\rho d V^2 C_{\mathrm{L}} - \frac{1}{2}\rho d C_{\mathrm{D}} V\frac{\partial y}{\partial t}. \tag{1}$$

Here, y represents the transverse deviation from a static position of the riser pipe. In the present linear theory, the riser is assumed to have a catenary shape in the static condition, and only the static component of the tension $T(s)$ is considered. We consider only the fluctuating lift force to simplify the theoretical analysis and elucidate the relationship between the lift force and structural motion, although in reality, potential and drag components also act. To bring a simulation of the dynamics of a riser more realistic such as [30], the drag as well as the lift must be considered, because it is one of the components inducing the vibration of the riser. This study pursues a clarification of the mechanical mechanism of the essence of the fluid–structure interaction along the riser, and thus employs a simplified model incorporating only the lift.

The time-varying lift force is described by a vibration equation with forcing by the acceleration in the y-direction as follows:

$$\frac{\partial^2}{\partial t^2}C_{\mathrm{L}} - 2\xi\omega_{\mathrm{v}}\left(1 - \frac{P'}{f^2}C_{\mathrm{L}}^2\right)\frac{\partial C_{\mathrm{L}}}{\partial t} + \omega_{\mathrm{v}}^2 C_{\mathrm{L}} = \frac{f}{\frac{1}{2}+l}\frac{\partial^2 y}{\partial t^2}, \tag{2}$$

which is the nonlinear wake oscillator model developed by [31]. When addressing the unmatured state of the VIV, the nonlinear term, the third order of magnitude of C_{L}, is negligible than the other terms, because in the unmatured state, C_{L} is quite smaller than unity. A mathematical proof for it is given in Appendix. This study thus employs a linearized form of Eq. (2) as follows:

$$\frac{\partial^2}{\partial t^2}C_{\mathrm{L}} - 2\xi\omega_{\mathrm{v}}\frac{\partial C_{\mathrm{L}}}{\partial t} + \omega_{\mathrm{v}}^2 C_{\mathrm{L}} = \frac{f}{\frac{1}{2}+l}\frac{\partial^2 y}{\partial t^2}. \tag{3}$$

The outputs of the model were validated and found to show reasonably good agreement with the measured displacements [31, 32] and hydrodynamic forces [33]. The vortex shedding frequency ω_{v} is related to the fluid velocity $V(s)$ as follows:

$$\omega_{\mathrm{v}} = 2\pi S_{\mathrm{t}}\frac{V}{d}, \tag{4}$$

where S_{t} denotes the Strouhal number, which is expressed in terms of dimensionless parameters of the wake oscillator as follows:

$$S_{\mathrm{t}} = \frac{1}{2}\sqrt{\frac{1}{\pi q^* k^*}}. \tag{5}$$

Without structural motion, the wake oscillator represents vortex shedding behind a fixed circular cylinder. It is characterized by the following dimensionless parameters:

$$l^* \equiv \frac{l}{d},\ k^* \equiv \frac{1}{2} + l^*,\ n^* \equiv \frac{\rho d^2}{2M\pi},\ \text{and } q^* \equiv \frac{q}{d}. \tag{6}$$

The notation k^* represents the radius of rotation of the wake oscillator.

Normalizing the quantities by M, L, and time defined as $\sqrt{L/g}$, we have the dimensionless forms of the governing Eqs. (1) and (3):

$$Y'' - \frac{\partial}{\partial s}\left\{\alpha(s)\frac{\partial Y}{\partial s}\right\} + E^*\frac{\partial^4 Y}{\partial s^4} = n^* k^* q^* \omega_{\mathrm{v}}^{*2} C_{\mathrm{L}} - n^* C_{\mathrm{D}}\sqrt{\pi q^* k^*}\,\omega_{\mathrm{v}}^* Y', \tag{7}$$

$$C_{\mathrm{L}}'' - 2\xi\omega_{\mathrm{v}}^* C_{\mathrm{L}}' + \omega_{\mathrm{v}}^{*2} C_{\mathrm{L}} = \frac{f}{k^*}Y''. \tag{8}$$

In Eqs. (7–8) and henceforth, s is used as a dimensionless quantity, and $\omega_{\mathrm{v}}^* \equiv \omega_{\mathrm{v}}\sqrt{L/g}$ is the dimensionless vortex shedding frequency. A prime symbol $'$ indicates a first-order differentiation with respect to dimensionless time. The dimensionless form of the static tension is assumed to be given by that of the catenary cable as follows:

$$\alpha(s) = \sqrt{a^{*2} + s^2}. \tag{9}$$

The imposed boundary conditions are that the riser is simply supported at both its extremities:

$$\begin{cases} Y(0) = Y''(0) = 0, \\ Y(1) = Y''(1) = 0. \end{cases} \tag{10}$$

Starting from Eqs. (7) and (8), we derive the energy equation for a coupled fluid–structure system as follows:

$$\begin{aligned}\frac{\partial}{\partial t}\left\langle \frac{1}{2}\left(Y'^2+\alpha(s)\left(\frac{\partial Y}{\partial s}\right)^2+K\left(\frac{\partial^2 Y}{\partial s^2}\right)^2 \right.\right.\\ \left.\left.+\frac{k^{*2}}{f^2}C_{\mathrm{L}}'^2+\omega_{\mathrm{v}}^{*2}\frac{k^{*2}}{f^2}C_{\mathrm{L}}\right)\right\rangle\\ =\underbrace{\left\langle n^*k^*q^*\omega_{\mathrm{v}}^{*2}C_{\mathrm{L}}Y'\right\rangle}_{FS}+\underbrace{\left\langle \frac{k^*}{f}Y''C_{\mathrm{L}}'\right\rangle}_{SF}\\ +\left\langle 2\xi\omega_{\mathrm{v}}^*\frac{k^{*2}}{f^2}C_{\mathrm{L}}'^2\right\rangle-\left\langle n^*C_{\mathrm{D}}\sqrt{\pi q^*k^*}\omega_{\mathrm{v}}^*Y'^2\right\rangle,\end{aligned} \tag{11}$$

where the bracket symbol <> means a spatial integration along the entire length of the riser pipe. The left-hand side of Eq. (11) represents the rate of variation in the dynamic energy contained in the coupled fluid–structure system.

The first and second terms on the right-hand side are the rate of energy transfer from the fluid to the structure (abbreviated as *FS*), and that from the structure to the fluid (abbreviated as *SF*), respectively. The FS term represents that a high correlation between C_{L} and Y' produces an energy delivery from the fluid to the structure, exciting the vibration of the riser pipe. A high correlation between C_{L} and Y' is mostly equivalent to a high correlation between Y'' and C_{L}'. This means that the energy transfer between the fluid and structure is interactive, and that the coupled system exhibits positive feedback. Following this concept, we examine how FS contributes during the growth phase of VIV to reveal the essential mechanism involved in the lift force elasticity of an underwater very long slender structure. The third term is the power extracted from the surrounding flow to the wake oscillator by the self-excitation property of the wake.

2.2 Structural eigenmodes

In this study, we also refer to structural eigenmodes as uncoupled modes to distinguish modes of the coupled fluid–structure system. Denoting the *i*th eigenfrequency by ν_i and the *i*th uncoupled mode function by y_i, they satisfy the freely vibrating beam equation with the above boundary conditions (Eq. 10):

$$-\nu_i^2 y_i(s)-\frac{\partial}{\partial s}\left\{\alpha(s)\frac{\partial y_i}{\partial s}\right\}+E^*\frac{\partial^4 y_i}{\partial s^4}=0. \tag{12}$$

To obtain a closed form of y_i with spatially varying tension $\alpha(s)$, we use one of the perturbation techniques to approximate it. Introducing a longer spatial coordinate defined as $z\equiv\epsilon s$ to view the order of variation of each term over the entire scale of the riser, Eq. (12) is recast into [27]:

$$\begin{aligned}-\omega_i^2 y_i(z)-\epsilon^2\alpha^*(z)\frac{\partial^2}{\partial z^2}y_i(z)-\epsilon\beta^*(z)\frac{\partial}{\partial z}y_i(z)\\ +\epsilon^5\frac{\partial^4}{\partial z^4}y_i(z)=0,\end{aligned} \tag{13}$$

where $\alpha^*(z)\equiv\alpha(z/\epsilon)$ and $\beta^*(z)\equiv\epsilon\frac{d\alpha^*(z)}{dz}$. In Eq. (13), the dimensionless bending stiffness E^* is selected as the book-keeping parameter ϵ, that is, $E^*=\epsilon$, because it is generally significantly smaller than unity.

The fourth term has the highest order derivative with the highest order of ϵ multiplied. Consideration of the bending stiffness and prevention of secular terms from appearing in the solution lead us to use a singular perturbation method. In this study, the Wentzel–Kramers–Brillouin (WKB) method was employed, because it is applicable if the functions $\alpha^*(z)$ and $\beta^*(z)$ can be regarded as slowly varying functions, that is, if they can be assumed to vary by the zeroth order of ϵ ($O(1)$) on a spatial scale of $O(1)$, which is the case for the present problem.

The WKB method expresses the solution as follows:

$$y_i(z)\sim\exp\left[\frac{1}{\epsilon}\sum_{n=0}^{\infty}\epsilon^n u_n(z)\right],\ \epsilon\to 0, \tag{14}$$

in which an asymptotic expansion in powers of ϵ appears in the argument of the exponential. The expansion coefficients u_n are determined by substituting the form of Eq. (14) into Eq. (13) and equating terms of the same order of ϵ [27].

The uncoupled mode functions approximately satisfy the following orthogonal relations:

$$\int_0^1 y_i(s)y_j(s)\mathrm{d}s=I_i\delta_{ij}, \tag{15}$$

where δ_{ij} is the Kronecker delta function, and I_i is *i*th nonzero value computed from the above integration.

2.3 Eigenfunction expansion and modal decomposition

Let the solution of the simultaneous equations (Eqs. 7, 8) be Y and C_{L}, which is the solution of the coupled fluid–structure system. Expansions of Y and C_{L} in terms of the uncoupled mode functions y_i are:

$$Y(s,\ t)=\sum_{i=1}^{N}Y_i(t)y_i(s), \tag{16}$$

$$C_{\mathrm{L}}(s,\ t)=\sum_{i=1}^{N}C_{\mathrm{L}\_i}(t)y_i(s). \tag{17}$$

The expansion in terms of mode functions for both the structural and fluid variables has been used by [29]. Substituting these expanded forms into the governing equations (Eqs. 7, 8), multiplying both by y_j, integrating them over $0 \le s \le 1$, and applying Eq. (15), we have:

$$\left(Y_j'' + v_j^2 Y_j\right) I_j = -n^* C_D \sqrt{\pi q^* k^*} V_{ji} Y_i' + \underbrace{n^* k^* q^* W_{ji} C_{L\_i}}_{FS}, \tag{18}$$

$$C_{L\_j}'' I_j - 2\xi V_{ji} C_{L\_i}' + W_{ji} C_{L\_i} = \underbrace{\frac{f}{k^*} Y_j'' I_j}_{SF}, \tag{19}$$

where V_{ji} and W_{ji} denote elements of the matrices $\mathbf{V}$ and $\mathbf{W}$ defined below, and i and j are integers that satisfy $1 \le i, j \le N$. In the above expressions, the Einstein summation convention is applied. In the subsequent subsections, an analytical way to address the fluid–structure interaction along the riser will be built, in which the matrices $\mathbf{V}$ and $\mathbf{W}$ have a key role.

2.4 Matrix representation of fluid–structure interaction

The $N \times N$ matrices $\mathbf{V}$ and $\mathbf{W}$ are defined as follows:

$$\mathbf{V} = (V_{ji}) \equiv \int_0^1 \omega_v^*(s) y_i(s) y_j(s) \mathrm{d}s, \tag{20}$$

$$\mathbf{W} = (W_{ji}) \equiv \int_0^1 \left\{\omega_v^*(s)\right\}^2 y_i(s) y_j(s) \mathrm{d}s, \tag{21}$$

where i and j represent column and row numbers, respectively. $\mathbf{V}$ and $\mathbf{W}$ are symmetric. The diagonal elements of $\mathbf{V}$ ($\mathbf{W}$) measure the extent to which the profile of the flow velocity (the profile of the flow velocity squared) overlaps with the configuration of the structural eigenmode function squared. The off-diagonal elements of $\mathbf{V}$ ($\mathbf{W}$) measure the correlation among the profile of the flow velocity (the profile of the flow velocity squared) and the ith and jth structural eigenmodes. Here, the matrices $\mathbf{V}$ and $\mathbf{W}$ are referred to as the first and second kinds of fluid–structure interaction (FSI) matrices, respectively.

To examine the solutions of Eqs. (18) and (19) using matrix algebra, they are written in a state space form. The state vector is defined as follows:

$$\mathbf{X} \equiv \left(\mathbf{Y}^{\mathrm{T}},\ \mathbf{C}_{\mathrm{L}}^{\mathrm{T}}\right)^{\mathrm{T}}, \tag{22}$$

$$\mathbf{Y} \equiv \left(Y_1,\ \ldots,\ Y_N\right)^{\mathrm{T}}, \tag{23}$$

$$\mathbf{C}_{\mathrm{L}} \equiv \left(C_{L\_1},\ \ldots,\ C_{L\_N}\right)^{\mathrm{T}}. \tag{24}$$

Equations (18) and (19) are second-order ordinary differential equations with respect to time. To reduce the differential order of the state space form, we define an augmented vector from $\mathbf{X}$ as follows:

$$\widetilde{\mathbf{X}} \equiv \left(\mathbf{X},\ \mathbf{X}'\right)^{\mathrm{T}}. \tag{25}$$

Equations (18) and (19) are thereby of the form:

$$\widetilde{\mathbf{X}}' = \mathbf{A}\widetilde{\mathbf{X}}, \tag{26}$$

where the state transition matrix $(4N \times 4N)$ $\mathbf{A}$ is defined as follows:

$$\mathbf{A} \equiv \begin{bmatrix} \mathbf{O} & \mathbf{E} \\ -\mathbf{K} & -\mathbf{C} \end{bmatrix}. \tag{27}$$

The $2N \times 2N$ submatrix $\mathbf{K}$ contains elements of restoring effects:

$$\mathbf{K} = \begin{bmatrix} \mathbf{K}_{\mathrm{SS}} & \mathbf{K}_{\mathrm{SF}} \\ \mathbf{K}_{\mathrm{FS}} & \mathbf{K}_{\mathrm{FF}} \end{bmatrix}, \tag{28}$$

where the $N \times N$ submatrices in $\mathbf{K}$ are defined as follows:

$$\mathbf{K}_{\mathrm{SS}} \equiv -\mathrm{diag}\left(v_j^2\right), \tag{29}$$

$$\mathbf{K}_{\mathrm{SF}} \equiv -n^* k^* q^* \mathrm{diag}\left(I_j^{-1}\right)\mathbf{W}, \tag{30}$$

$$\mathbf{K}_{\mathrm{FS}} \equiv \frac{f}{k^*}\mathbf{K}_{\mathrm{SS}}, \tag{31}$$

$$\mathbf{K}_{\mathrm{FF}} \equiv (1 - fn^* q^*)\mathrm{diag}\left(I_j^{-1}\right)\mathbf{W}. \tag{32}$$

The $2N \times 2N$ submatrix $\mathbf{C}$ contains elements of damping and self-excitation effects:

$$\mathbf{C} = \begin{bmatrix} \mathbf{C}_{\mathrm{SS}} & \mathbf{O} \\ \mathbf{C}_{\mathrm{FS}} & \mathbf{C}_{\mathrm{FF}} \end{bmatrix}, \tag{33}$$

where the $N \times N$ submatrices in $\mathbf{C}$ are defined as follows:

$$\mathbf{C}_{\mathrm{SS}} \equiv -n^* C_D \sqrt{\pi q^* k^*}\mathrm{diag}\left(I_j^{-1}\right)\mathbf{V}, \tag{34}$$

$$\mathbf{C}_{\mathrm{FS}} \equiv \frac{f}{k^*}\mathbf{C}_{\mathrm{SS}}, \tag{35}$$

$$\mathbf{C}_{\mathrm{FF}} \equiv 2\xi \mathrm{diag}\left(I_j^{-1}\right)\mathbf{V}. \tag{36}$$

2.5 Eigenvalue analysis on coupled fluid–structure system

Assuming that the temporal variation in $\widetilde{\mathbf{X}}$ is expressed as $\overline{\mathbf{X}}e^{\lambda t}$, we derive from Eq. (26) an eigenvalue problem as follows:

$$\mathbf{A}\overline{\mathbf{X}} = \lambda\overline{\mathbf{X}}. \tag{37}$$

Whether the vibration of a mode grows or not is indicated by the real part of the eigenvalues. A positive (negative) real part corresponds to the growth (evanescence) of the mode.

Letting the state vector at an initial condition at a time of t_0 be $\widetilde{\mathbf{X}}_0$, the solution of the above equation is expressed in the matrix exponential form as follows:

$$\widetilde{\mathbf{X}} = e^{\mathbf{A}(t-t_0)}\widetilde{\mathbf{X}}_0. \tag{38}$$

Denoting the eigenvectors and eigenvalues of the eigenvalue problem by $\mathbf{p}_i$ and λ_i, respectively, the similarity transformation of $\mathbf{A}$ is written as follows:

$$\begin{aligned}&\left[\mathbf{p}_1\ \mathbf{p}_2\ \cdots \mathbf{p}_{4N}\right]^{-1}\mathbf{A}\left[\mathbf{p}_1\ \mathbf{p}_2\ \cdots \mathbf{p}_{4N}\right]\\ &\quad = \mathrm{diag}\left[\lambda_1\ \lambda_2 \ldots \lambda_{4N}\right].\end{aligned} \tag{39}$$

By applying Eq. (39), the above solution can be expanded in terms of the eigenvectors as follows:

$$\begin{aligned}\widetilde{\mathbf{X}} &= \sum_{k=1}^{4N}\mathbf{p}_k\mathbf{q}_k^{\mathrm{T}}\widetilde{\mathbf{X}}_0 e^{\lambda_k t}\\ &= \sum_{k=1}^{4N} m_k e^{\lambda_k t}\mathbf{p}_k,\end{aligned} \tag{40}$$

where the vectors $\mathbf{q}_k$ are defined as follows:

$$\left[\mathbf{p}_1\ \mathbf{p}_2\ \cdots \mathbf{p}_{4N}\right]^{-1} \equiv \begin{bmatrix}\mathbf{q}_1^{\mathrm{T}}\\ \mathbf{q}_2^{\mathrm{T}}\\ \vdots\\ \mathbf{q}_{4N}^{\mathrm{T}}\end{bmatrix}, \tag{41}$$

and the scalar quantities m_k are the inner product between $\mathbf{q}_k$ and $\widetilde{\mathbf{X}}_0$, expressed as follows:

$$m_k \equiv \mathbf{q}_k^{\mathrm{T}}\widetilde{\mathbf{X}}_0. \tag{42}$$

The eigenvectors are generally complex and are written using the real numbers p_{k_i} and ϕ_{k_i} as follows:

$$\mathbf{p}_k = \left[p_{k\_1}e^{\mathrm{i}\phi_{k\_1}} \ldots p_{k\_4N}e^{\mathrm{i}\phi_{k\_4N}}\right]^{\mathrm{T}}, \tag{43}$$

and therefore, the components of displacement and lift and their temporal differentiations are expressed as follows:

$$\widetilde{\mathbf{X}} = \sum_{k=1}^{4N} m_k\left[p_{k\_1}e^{\lambda_k t+\mathrm{i}\phi_{k\_1}}\ \ldots p_{k\_4N}e^{\lambda_k t+\mathrm{i}\phi_{k\_4N}}\right]^{\mathrm{T}}. \tag{44}$$

Equation (44) represents that the real parts of the eigenvalues λ_k specify which coupled modes will grow, and that p_{k_i}, the magnitudes of the eigenvectors, specify which uncoupled modes will be the most dominant with a certain frequency given as the imaginary part of λ_k. The $4N$ components of $\mathbf{p}_k$ correspond to $\mathbf{Y}$ $(i = 1, \ldots, N)$, $\mathbf{C}_{\mathrm{L}}$ $(i = N+1, \ldots, 2N)$, $\mathbf{Y}'$ $(i = 2N+1, \ldots, 3N)$, and $\mathbf{C}'_{\mathrm{L}}$ $(i = 3N+1, \ldots, 4N)$.

In Sect. 3.4, we will take only the most unstable component into consideration to discuss the energetics of the coupled system. This treatment is equivalent to considering only a single component of frequency that is the most dominant, retaining the complex conjugate pair with the largest real part of the eigenvalue. Now, let the integer k that corresponds to the largest real part be denoted by K. The above approximation is expressed as follows:

$$\widetilde{\mathbf{X}} \simeq m_K e^{\lambda_K t}\mathbf{p}_K + \mathrm{c.c.}, \tag{45}$$

where c.c. means complex conjugate.

2.6 Modally decomposed rigid bodies

Under a uniform profile of flow, all modes become independent of each other, whereby interactions between the fluid and structure are made within the same mode. The equations of all the modes are completely decomposed, because the FSI matrices become diagonal, and are reduced to:

$$\begin{aligned}Y_j'' + \nu_j^2 Y_j = &-n^* C_{\mathrm{D}}\sqrt{\pi q^* k^*}\,\omega^*_{\mathrm{v}\,0}Y_j'(t)\\ &\underbrace{+\,n^* k^* q^*\left(\omega^*_{\mathrm{v}\,0}\right)^2 C_{\mathrm{L}\_i}(t)}_{FS},\end{aligned} \tag{46}$$

$$C''_{\mathrm{L}\_j} - 2\xi\omega^*_{\mathrm{v}\,0}C'_{\mathrm{L}\_j} + \left(\omega^*_{\mathrm{v}\,0}\right)^2 C_{\mathrm{L}\_j} = \underbrace{\frac{f}{k^*}Y_j''}_{SF}, \tag{47}$$

where $\omega_{\mathrm{v}\,0}$ denotes the dimensionless uniform velocity. Equations (46) and (47) are equivalent to the set of equations for a rigid circular cylinder.

Writing a complex eigenvalue as $\lambda = \lambda_{\mathrm{R}} + \mathrm{i}\lambda_{\mathrm{i}}$, we can relate ϕ, the phase of C_{L_j} relative to that of Y_j, to the real and imaginary parts of the eigenvalue as follows:

$$\begin{aligned}\tan\phi &= \frac{\left(2\lambda_{\mathrm{R}} + D\right)\lambda_{\mathrm{i}}}{\lambda_{\mathrm{R}}^2 - \lambda_{\mathrm{i}}^2 + D\lambda_{\mathrm{R}} + \nu_j^2},\\ D &\equiv n^* C_{\mathrm{D}}\sqrt{\pi q^* k^*}\,\omega^*_{\mathrm{v}\,0}.\end{aligned} \tag{48}$$

When a *j*th mode greatly grows, the *j*th mode lift force is expected to have a phase that favors the growth of the *j*th structural mode, making $\tan\phi$ quite large. Letting the value of $\tan\phi$ be denoted by p, the following relationship is derived as follows:

$$\lambda_{\mathrm{R}}^2 - \frac{2}{p}\lambda_{\mathrm{R}}\lambda_{\mathrm{i}} - \lambda_{\mathrm{i}}^2 + D\lambda_{\mathrm{R}} - \frac{D}{p}\lambda_{\mathrm{i}} + \nu_j^2 = 0. \tag{49}$$

Equation (49) expresses the constraint condition satisfied by λ_{R} and λ_{i}, and, on the λ_{R}–λ_{i} plane, it represents many hyperbolic curves as the eigenmode number j varies. The left-hand side of Eq. (49) is the quadratic form in terms of $(\lambda_{\mathrm{R}},\ \lambda_{\mathrm{i}})$. Through the following orthogonal transformation:

$$\begin{bmatrix} u \\ v \end{bmatrix} = \mathbf{P}^{\mathrm{T}} \begin{bmatrix} \lambda_{\mathrm{R}} \\ \lambda_{\mathrm{i}} \end{bmatrix}, \tag{50}$$

$$\mathbf{P} \equiv \begin{bmatrix} 1 & -p\left(1-\sqrt{1+p^{-2}}\right) \\ p\left(1-\sqrt{1+p^{-2}}\right) & 1 \end{bmatrix}, \tag{51}$$

the above hyperbolic curves are transformed into their standard forms as follows:

$$\frac{\left(u+\frac{1}{2}D\right)^2}{\frac{\nu_j^2}{\sqrt{1+p^{-2}}}} - \frac{\left(v+\frac{1}{2}D\right)^2}{\frac{\nu_j^2}{\sqrt{1+p^{-2}}}} = -1, \tag{52}$$

which represents the hyperbolic curves with their focal points at $\left(-\frac{1}{2}D,\ \pm\frac{\sqrt{2}\nu_j}{\sqrt[4]{1+p^{-2}}} - \frac{1}{2}D\right)$ in the u–v coordinate system (e.g., [34]). Those hyperbolic curves have the common asymptotic lines expressed as follows:

$$v + \frac{1}{2}D = \pm\left(u + \frac{1}{2}D\right). \tag{53}$$

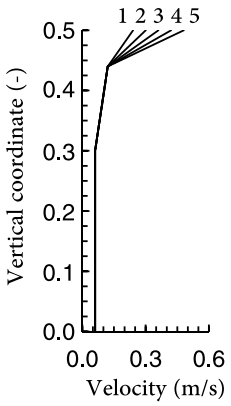

Fig. 1 Vertical profiles of flow velocities for Cases 1–5. Vertical coordinate is normalized by the total length of the riser

2.7 Computational conditions

In this study, several vertical profiles of the flow velocity were constructed by referring to published data obtained from oceanographic observations [18, 35, 36] in the Gulf of Mexico, and simulated using a numerical ocean model [37] applied to the Brazilian Equatorial Margin. The Gulf Stream and the North Brazil Current are present at the former and latter sites, respectively. The vertical profiles at both sites have the following elements in common: prominent shears are formed from the surface to a depth of a few hundred meters because of the very strong currents, below which relatively weak shears are observed to 1000 m. Below the strong and weak shear layers, there are layers with almost uniform profiles. In Fig. 1, five examples of vertical profiles of the flow velocity are plotted. Those are substituted into the fluid velocity V, which thus depends on s and, accordingly, ω_{v} also depends on s.

The production riser treated in this study is installed at a site with a depth of 2500 m, with a catenary configuration and a total length of 5000 m. The catenary configuration is shown in Fig. 2, in which the horizontal and vertical coordinates are normalized.

To calculate the integrals in Eqs. (20) and (21), Simpson's formula was adopted. The number of mode expansion N was determined considering the eigenvalues computed and memory needed for the computation.

3 Results and discussion

3.1 Validation

To validate the numerical computations, the computed eigenfrequencies are compared in Fig. 3 with those measured in the experiment by [38], in which a horizontal riser model with a length of 28.04 m and with a diameter of 0.016 m was subjected to flows. For lower eigenmodes, the present method exhibits good agreement with the experiment; however, the method tends to overestimate for the higher modes. The difference between the present analysis and the experiment is probably attributable to the algorithm in the WKB

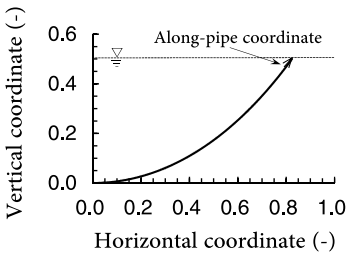

Fig. 2 Configuration of steal catenary riser considered in this study

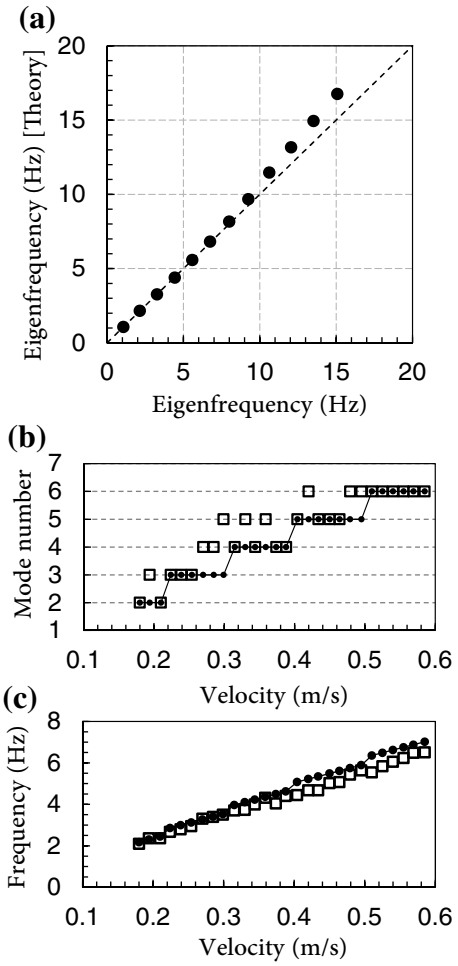

Fig. 3 Comparison of present analysis with the experiment [38]. **a** Eigenfrequency, **b** dominant mode number against flow velocity, and **c** dominant frequency against flow velocity. In **b** and **c**, the closed circles are computed results, and opened squares are experimental results

approximation. We guess that, for a small-sized model, the accuracy of the asymptotic expansion decreases, because the bookkeeping parameter ϵ is not so small.

The experiment [38] shows that the most dominant mode gradually becomes higher as the flow velocity increases. The computation reproduced it well (Fig. 3). The measured frequencies of vibration also show increasing variations with increasing flow velocity, which agreed fairly well with the computations. However, for the flow velocities ranging from 0.4 to 0.6 m s^{-1}, the computation produced larger frequencies than the measured ones. These discrepancies may be attributed to the above-mentioned eigenfrequency overestimations, which probably lead also to the appearances of the lower modes in the computations (Fig. 3b). However, because the computations of the eigenfrequencies (Fig. 3a) and dominant frequencies (Fig. 3c) for the lower velocity cases (0.2–0.4 m s^{-1}) agree fairly well with the experiments,

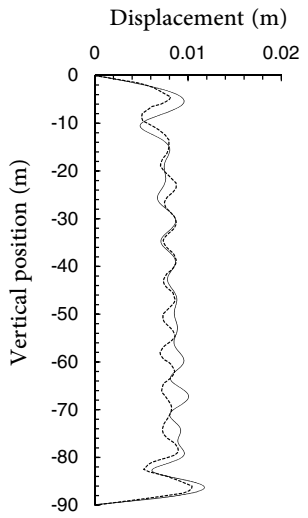

Fig. 4 Vertical distribution of root mean squares of displacements (towing speed of 0.54 m s^{-1}). The solid line is computed results and dashed one is measured results [39]

another factor as well as the eigenfrequency overestimations should be considered to account for the lower modes in the computations: for example, the linear model may not sufficiently capture transitions between neighboring modes which irregularly occur in the experiments.

To furthermore validate the model used in this study, a solution of the nonlinear form of the model (Eqs. 1, 2) was numerically computed in the time domain. The computed results were compared in Fig. 4 with the experimental data [39] measured using a straight riser model with a length of 90 m and with a diameter of 0.03 m. The experimental riser model was subjected to a linearly sheared flow by towing the model in a test tank. This comparison shows that the analytical model reasonably well reproduces the real phenomenon.

The validations shown above were for the experimental models which had much smaller scales than the risers installed in the actual ocean. The subsequent section targets the actual size. Although the validity of the analytical model shown here does not fully ensure it for the actual

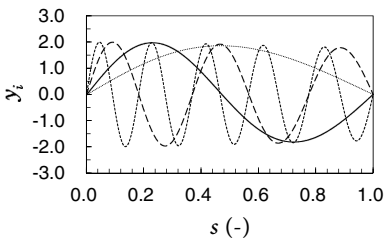

Fig. 5 Transverse components of eigenfunctions obtained from the WKB method. The first, second, fifth, and tenth eigenfunctions are plotted

scale, the analytical model used in this study is described in terms of the dimensionless variables and parameters, and thus is applicable without considering the scale. We should, however, be careful for variations of the parameters depending on the scale. As for this regard, separate considerations are needed.

3.2 Structural eigenmode function

The computed structural eigenmode functions are plotted in Fig. 5. Their spatial variation is quite similar to that of sinusoidal functions, while their amplitudes very slowly increase toward the bottom end because of the effect of the third term of Eq. (13) including $\beta^*(z)$.

3.3 Response in uniform flow

Figure 6 plots the computed eigenvalues against the dimensionless fluid velocity. The positive values of the real part indicate the growth of VIV. With the dimensionless velocities ranging from 4.0 to 6.5, the growth can be detected, and the frequencies are close to the eigenfrequency, which means the occurrence of frequency lock-in to the natural frequency. Larger velocities inhibit the growth. Negative real parts of eigenvalues represent evanescence of the modes, and are unobservable.

Under the uniform flow condition, there is no interference among different modes, that is, all of the modes are independent to each other, while interactions between the fluid and structure take place only within the same mode. This is mathematically represented by diagonal configurations of the matrices **V** and **W**.

To understand how the lift forces and structural motions interact with each other and eventually grow the VIV, the phases of lift forces relative to those of the displacements are calculated using eigenvectors (Fig. 6c). The most unstable mode has the phase of almost 90°. This condition in which the lift force gives positive works to the structure and concurrently the structural motion gives positive works to the wake. This study refers to the former force as FS force, that is, the force acting from the fluid to structure, and the latter force as SF force, the force acting from the structure to fluid.

Energetics of the coupled fluid–structure system provides us with a clearer insight about the interaction. The power of the FS force increases if the lift force has positive correlation with the velocity of structural motion, as expressed in the right-hand side of Eq. (46). We should note that the maximization of the power of the FS force is accompanied by the maximization of the power of the SF force, which is maximized if the velocity of the lift force variation has negative correlation with the displacement of structural motion. The lift force and structural displacement grow, tracing a divergent circulation on a $Y - C_L$ phase diagram (Fig. 7).

In the uniform flow case, the second kind FSI matrix is diagonal (Fig. 8a). Both the structural (Fig. 8b) and lift force (Fig. 8c) modes have the single peak at the mode numbers corresponding to the diagonal elements, accordingly yielding the peak of FS power (Fig. 8d). The other elements of FS power are negative, meaning that those elements serve

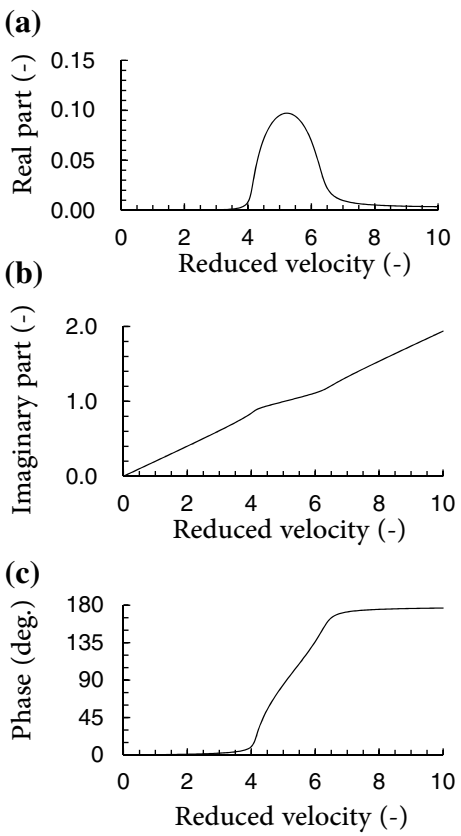

Fig. 6 Solution of a mode in uniform flow case. **a** Real parts of eigenvalue, **b** imaginary parts of eigenvalue, and **c** phase of lift force relative to displacement of structural motion. Horizontal axis is reduced velocity

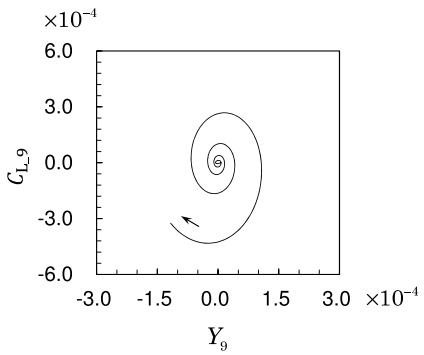

Fig. 7 Phase diagram of $Y - C_L$ in uniform flow case

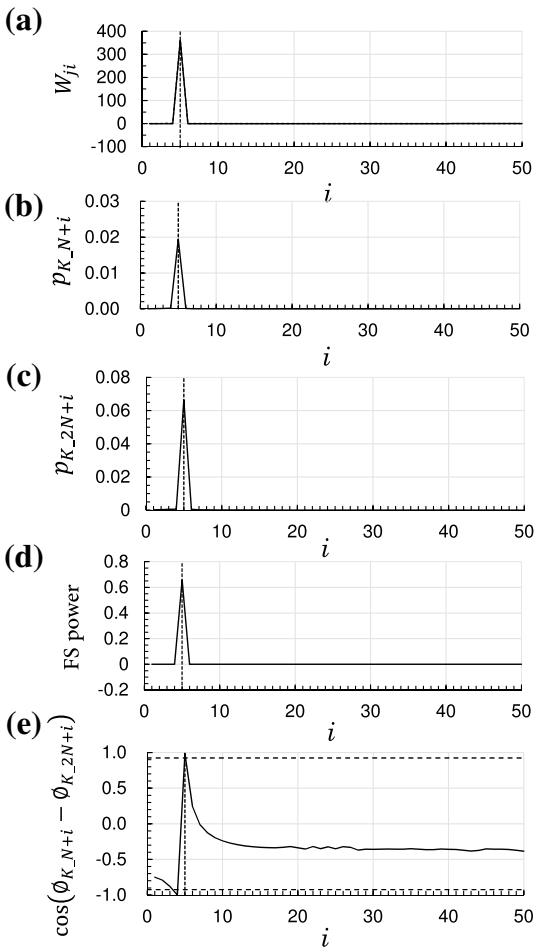

Fig. 8 Uniform flow case. **a** Elements of the second kind FSI matrix on the row corresponding to the most unstable structural mode Y_j, **b** p_{K_2n+i}, elements of eigenvector of the structural mode, **c** p_{K_n+i}, elements of eigenvector of the lift force mode, **d** FS power from each lift force mode C_{L_i} to Y_j, and **e** cosine function of phase of C_{L_i} relative to that of Y_j' (horizontal dashed lines are cosine functions of phase calculated by rigid body approximation). Vertical lines indicate the jth elements. In **a**–**e**, horizontal axis is the lift force mode number, i

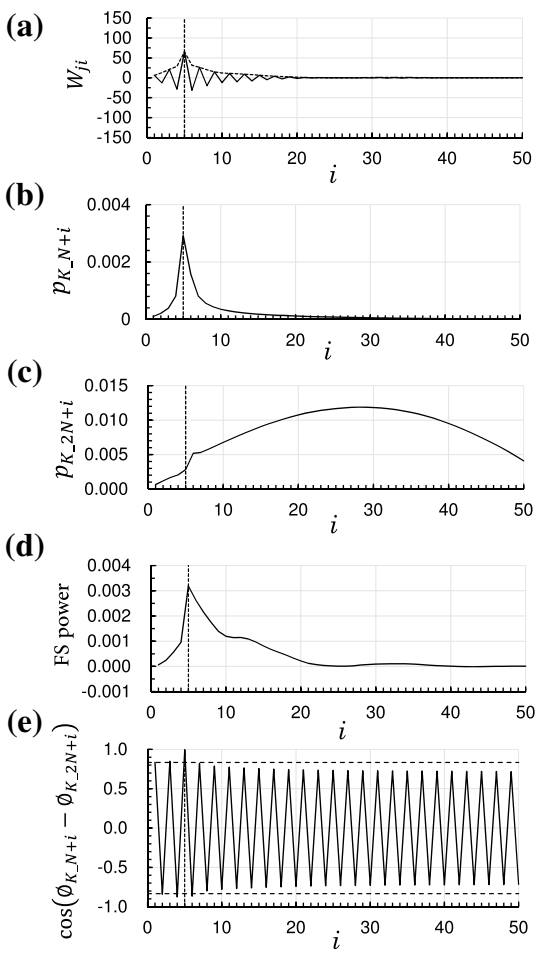

Fig. 9 Case 1. **a** Elements of the second kind FSI matrix on the row corresponding to the most unstable structural mode Y_j, **b** p_{K_2N+i}, elements of structural mode eigenvector, **c** p_{K_N+i}, elements of lift force mode eigenvector, **d** FS power from each lift force mode C_{L_i} to Y_j, and **e** cosine function of phase of C_{L_i} relative to that of Y_j' (horizontal dashed lines are cosine functions of phase calculated by rigid body approximation). Vertical lines indicate the jth elements. In **a**–**e**, horizontal axis is the lift force mode number, i

as the energy conveyers from the coupled system to the surrounding current.

The above interpretation of the VIV growth can be thought to be a dynamic instability induced by the coupling between the fluid and structural dynamics. The instability caused by the coupled fluid–structure interaction is made through FS and SF forces. The dynamic instabilities similar to the one addressed in this study have been identified in other coupled systems: a coupled mechanics in the atmosphere–ocean system in the tropics produces a source of global climate events [40], a coupled sea–ice–ocean system explains well ice melting in the Antarctic [41], high-speed stability of a driver–motorcycle system, [42], and a coupled strip–roll system in a cold rolling mill [43]. These studies are from a variety of academic areas and, nevertheless, have in common the mathematical background that describes this type of instability.

3.4 Energetics in shear flow

Next, we closely examine the rate of work done by the FS term in Eq. (18) (hereinafter, it is referred to as FS power) to determine the instability of the coupled fluid–structure system in shear flows. Here, a single-frequency approximation is applied, which is written as Eq. (45). Under this approximation, the FS power can be calculated by multiplying Eq. (18) by Y_j' and by averaging the result over one period.

The presence of shears in a flow velocity profile makes the off-diagonal elements of FSI matrices nonzero. Those off-diagonal elements are alternately positive and negative. This is because the neighboring uncoupled mode shapes are even and odd (Fig. 5). Figure 9a shows elements of the second kind FSI matrix on the fifth row for case 1, in which the fifth structural eigenmode grows the most rapidly (Fig. 9b). A sharp maximum in FS power (Fig. 9d) indicates that the fifth lift mode supplies the largest amount of energy with the fifth structural eigenmode.

It is noteworthy that $C_{\mathrm{L\_5}}$ is not the only mode that supplies Y_5 with energy (Figs. 9c and d). Cosine functions of phase of $C_{\mathrm{L\_}i}$ relative to Y' (Fig. 9e), which are a factor determining the magnitude of the FS power, has alternately positive and negative values. This distribution of the cosine functions comes from the zigzag arrangement of the elements in the second kind FSI matrix. These indicate that higher modes of $C_{\mathrm{L\_}i}$ remarkably contribute the energy supply to the fifth structural eigenmode, making the FS power have positive values over a wide range of the $C_{\mathrm{L\_}i}$ mode number. The clockwise and anti-clockwise trajectories in Fig. 10 are explained by the phase lead and delay, i.e., the alternate reverses of the cosine functions of phase.

A stronger shear (Case 5) provides an interesting FS power distribution (Fig. 11d). The most rapidly growing mode of the displacement is Y_{10} (Fig. 11b), while it is $C_{\mathrm{L\_11}}$ that gives Y_{10} with energy. The lift force includes several higher modes that grow (Fig. 11c), creating gentle slopes in the FS power (Fig. 11d).

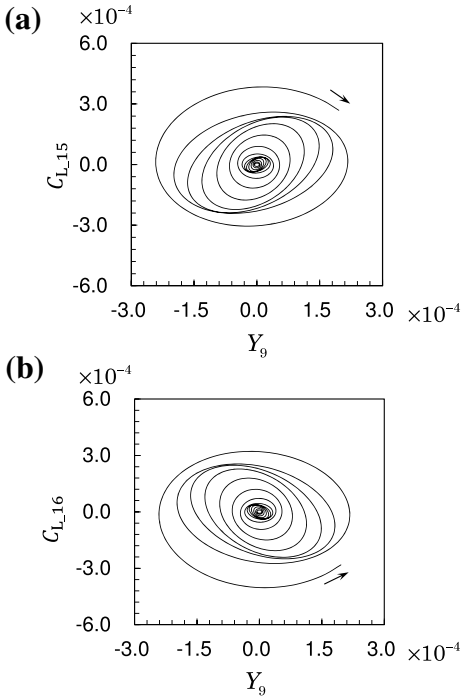

Fig. 10 Phase diagram for Case 1. **a** $Y_9 - C_{\mathrm{L\_15}}$ and **b** $Y_9 - C_{\mathrm{L\_16}}$

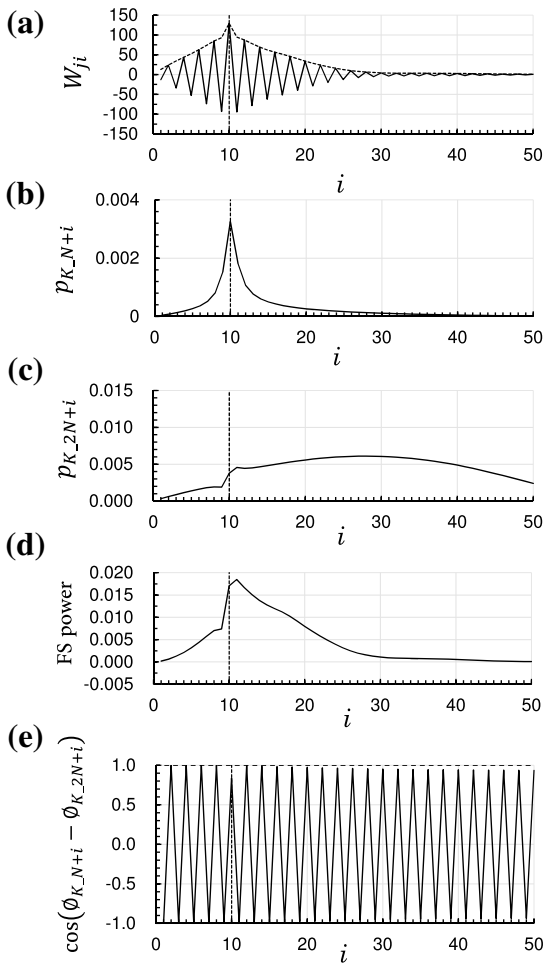

Fig. 11 Case 5. **a** Elements of the second kind FSI matrix on the row corresponding to the most unstable structural mode Y_j, **b** p_{K_2N+i}, elements of eigenvector of structural mode, **c** p_{K_n+i}, elements of eigenvector of lift force mode, **d** FS power from each lift force mode $C_{\mathrm{L\_}i}$ to Y_j, and **e** cosine function of phase of $C_{\mathrm{L\_}i}$ relative to that of Y_j' (horizontal dashed lines are cosine functions of phase calculated by rigid body approximation). Vertical lines indicate the jth elements. In **a**–**e**, horizontal axis is the lift force mode number, i

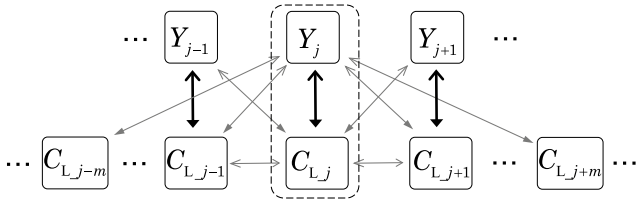

Fig. 12 Schematic view of energy deliveries around structural mode Y_j. Arrows indicate energy deliveries. In uniform flow case, energies are interchanged inside dashed boxes

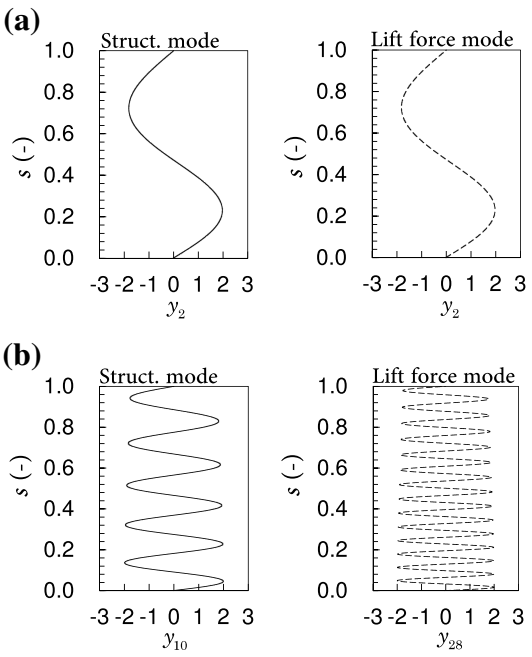

Fig. 13 Coexistence of lower structural mode and higher lift force mode. **a** Uniform flow (0.2 m s^{-1}) case, and **b** Shear flow case (Case 5). In **a**, **b**, the modes corresponding to the largest magnitude of elements in eigenvector are depicted

The energy deliveries in the shear flows significantly differ from that in the uniform flow. It is of importance that the higher lift force modes contribute to the growth of lower structural modes, as schematically drawn in Fig. 12.

It is notable that several elements of the lift force eigenvector (Figs. 9c, 11c) have large values as well as the diagonal elements. These growths of lift force are seen especially in the modes higher than the diagonal one. These demonstrate that in the sheared flows, a single or more than one structural modes grow together with a lot of higher lift force modes.

Lower structural modes coexist with higher lift force modes (Fig. 13). The underlying physics can be explained from the viewpoint of modal decomposition. The vertical profile of the flow velocity (Fig. 1) has configurations much different from the configurations of the structural eigenmode functions (Fig. 5). The eigenmode functions consist of sinusoidal ones, which are even or odd looking from the central point of the pipe. The sheared profiles monotonically increase toward the water surface. The presence of a shear, even if it is weak one, accordingly needs a lot of low and high eigenmodes to be superimposed to reconstruct the profile including the shear. That is why the off-diagonal elements become nonzero, although they are far from the diagonal region.

The property of the lift force variation changes sensitively against the presence of a shear through the restoring terms $\mathbf{K}_{\mathrm{FF}}$, which is proportional to the second kind FSI matrix (Eq. 32). The nonzero off-diagonal elements of $\mathbf{W}$ produce interferences among different lift force modes. The oscillatory swinging motions of wake along the riser subject to a shear flow naturally exhibit multiple frequencies, enabling resonances among various lift force modes to occur, and consequently producing the growths of higher lift force modes. This differs significantly from the restoring property of wake formed in a uniform flow or wake behind a rigid circular cylinder, which can be characterized by a single Strouhal number.

This discussion on the lift force mode leads us to suppose that multiple high structural modes are likely to more considerably grow because of the excitation by the corresponding high lift force modes. Our analysis certainly shows the transfer of the dominantly growing structural mode toward a higher one (Figs. 9b, 11b). However, this transfer occurs at a much slower pace compared to the very rapid transfer of the lift force modes. The key factor lies in the restoring submatrix $\mathbf{K}_{\mathrm{SS}}$, which stays diagonal and is independent of the flow field. The influence of a shear in flows is given to the structural mode indirectly through the external force, the FS term, while it directly alters the internal forces (the third term in the left-hand side of Eq. 19) acting on the lift force mode.

3.5 Total energy supplied by all frequency components

The previous subsection discusses the FS power by taking only the most unstable frequency component (Eq. 45). Real responses of the displacement and lift force include many frequency components. Thus, applying Eq. (44) instead of Eq. (45) to superpose all of the frequency component of the calculated $\mathbf{C}_{\mathrm{L}}$ and $\mathbf{Y}'$, and integrating them in the time domain, we evaluated the total energy received by Y_j through the FS power over the integration period. For the five cases, the results of the calculations are shown in Fig. 14.

In Case 1, the energy tends to be concentrated on Y_5. By contrast, In Cases 2 and 3, the energy is supplied to two or more modes. The calculations for Cases 4 and 5 show that Y_9 and Y_{10} are supplied distinctively large amounts of the energy. These indicate that shear strength influences how many modes will grow. This aspect will be discussed again in the next subsection from a different point of view. In the five cases, moderate shear cases (Cases 2 and 3) tend to include more than one mode.

In the discussion in Sect. 3.4, Eq. (45) was applied. This approximate expression of the solution is derived by comparing the real parts of eigenvalues and omitting the

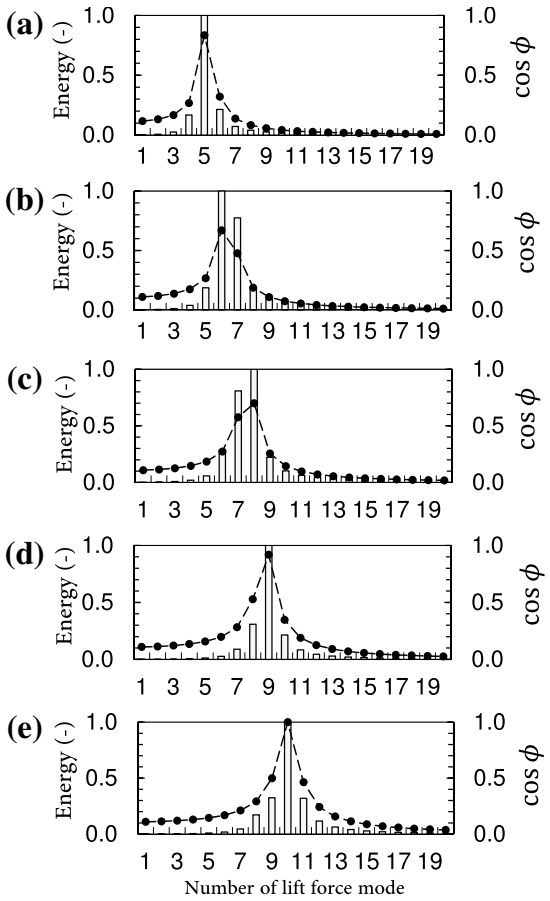

Fig. 14 Heights of bars represent the total energy supplied to each structural mode through the FS term. The subfigures **ae** correspond to Cases 1–5, respectively. The magnitudes of the energies are normalized by their maximum. Dashed line with circles indicates cosine function of the phase of C_{L_j} and Y'_j calculated by the rigid body approximation, where j denotes here, the number of the structural mode supplied with the maximum amount of energy

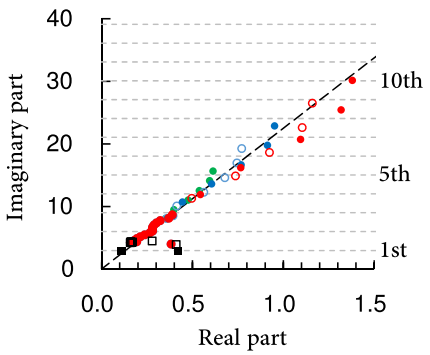

Fig. 15 Relationships of real (horizontal axis) and imaginary (vertical axis) parts of the eigenvalues for shear flow: Case 1 (closed green), 2 (opened blue), 3 (closed blue), 4 (opened red), and 5 (closed red). The same relationships for the uniform flow cases (0.04 m s^{-1}, closed square) (0.06 m s^{-1}, opened square) are also plotted. The dashed line shows the same relationship calculated by the rigid body approximation

secondary and subsequent components. Here, we examine whether this treatment is appropriate.

The phases calculated using the rigid body approximation (horizontal dashed lines in Figs. 9e, 11e) are in good agreement with those determined from the eigenvectors. The mode Y_j grows while being supplied the energies from other many modes of the lift force C_{L_i}. Although this pattern of energy delivery is quite different from that for the case of uniform flow (Fig. 8), the phase for the shear cases is very close to those computed under the rigid body approximation. This also applies to the total energy delivery to Y_j. The cosine functions of the phase are distributed similar to the total energies (Fig. 14).

3.6 Dominance of multiple frequency components

As discussed above, a shear profile of the flow velocity leads to the growths of certain components. Looking at them in terms of the real and imaginary parts of the eigenvalue, we identify them as remarkably large real parts (Fig. 15). Much attention should be paid to those real parts arranged seemingly in proportion to their corresponding imaginary parts. We offer a proof for the

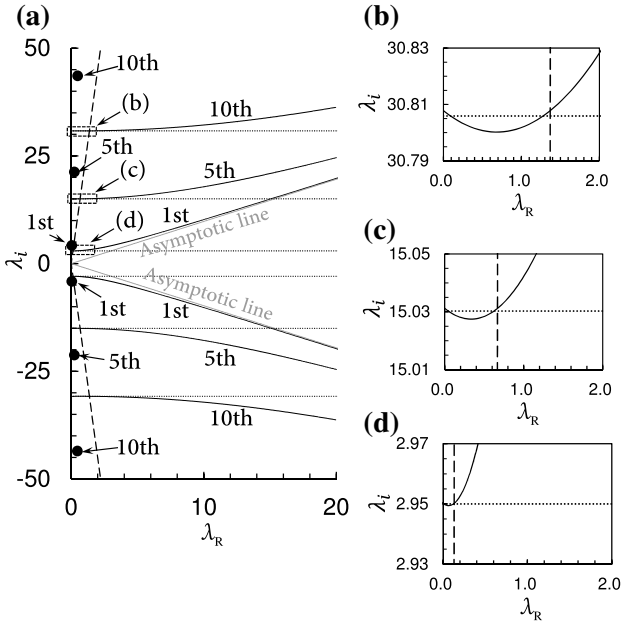

Fig. 16 **a** Plots of hyperbolic curves (solid curves) representing the relationship between λ_R and λ_i. Those for the first, fifth, and tenth modes are plotted. Horizontal dotted lines indicate the eigenfrequencies of each mode. Gray solid lines are asymptotic lines, and black circles are focal points. Black dashed line shows the same relationship calculated by the rigid body approximation with limit of $|p| \gg 1$. The three right panels, **b** 10th, **c** 5th, and **d** 1st, are enlargements at the intersections

relationship between λ_R and λ_i with the aid of the rigid body approximation.

The hyperbolic curves (Eq. 49) are slightly rotated from the standard ones (Eq. 52) by the orthogonal transformation (Eq. 50), and thus are intersected at two points by the horizontal line $\lambda_i = \nu_j$. Of the two intersections, that with a larger horizontal coordinate corresponds to the solution for lock-in to the jth eigenmode. All of the hyperbolic curves have the common asymptotic line (Fig. 16), while their focal points are located closer to the origin as j becomes smaller. If λ_i is positive, the convex downward curves near the focal point for a small j have a quite narrow valley shape. This geometrical fact shows that as j decreases, the real part of the lock-in solution decreases (the intersection of the solution is located closer to the vertical axis). We can also prove that these intersections form a line (Fig. 16) for the limit of $|p| \gg 1$.

Even if shears are present in the flow profiles, the growth of VIV in each frequency component can be reasonably well approximated by the modally decomposed rigid bodies. The relationships between the real and imaginary parts are depicted on the $\lambda_R - \lambda_i$ plane for the sheared flow cases (Fig. 15). When the real parts are much larger than zero, in other words, when the VIV of the modes is expected to grow, those real parts are in proportion to the imaginary parts. Considering the same relationship determined from the intersections on the hyperbolic curves on the same plane, we can see that both the relationships agree well. The plots for the sheared flows fluctuate slightly, stemming from the contributions by the interference of other modes through the off-diagonal elements of the FSI matrices.

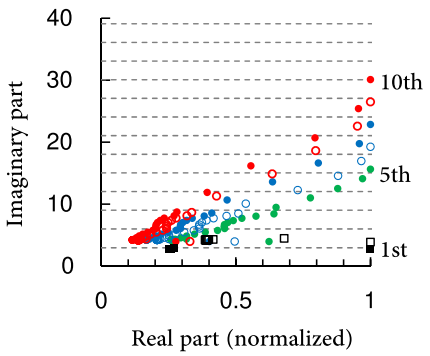

Fig. 17 Relationships of real (horizontal axis) and imaginary (vertical axis) parts of eigenvalues for shear flow. Real parts are normalized by their maxima: Case 1 (closed green), 2 (opened blue), 3 (closed blue), 4 (opened red), and 5 (closed red). The same relationships for uniform flow cases (0.04 m s^{-1}, closed square) and (0.06 m s^{-1}, opened square) are also plotted

The above discussion on the eigenvalue can be deepened by normalizing the real parts by their maxima to provide a clear insight on the dominance of multiple frequency components in shear flows (Fig. 17). With a relatively weak shear, the secondary and certain subsequent real parts are not so much smaller than the primary one. By contrast, stronger shears yield larger differences among the real parts. Those differences are related to the differences in the imaginary parts, as examined above.

The differences in the imaginary parts result from the shape of the magnitudes of the second kind FSI matrix. A comparison of them (Figs. 9a, 11a) demonstrates that the stronger shear gives the sharper inclination of the magnitudes with the larger peak at the diagonal position. With the sharper inclination of the magnitudes arranged in the second kind FSI matrix, the influence of the secondary and subsequent imaginary parts on the restoring property of the wake oscillation decreases relative to that of the primary imaginary part. The differences in the imaginary parts between neighboring growing modes become greater than they do in the weaker shear. This intensifies the tendency of the primary component to grow in an isolated manner. Although the present linear theory cannot sufficiently reproduce the frequency lock-in, the above result suggests the dominance of a single-frequency component under a strong shear flow condition.

This transfer of frequency component dominance is qualitatively consistent with the experimental finding by [19] and a numerical simulation in the time domain [28]: they showed that there is a range of shear strength within which multiple frequency components are observed at the same time, and that a shear beyond the range produces a single-frequency component that distinctively grows. However, our discussion is based on a linear theory, which cannot simulate the matured state of VIV, including the switch of the dominant mode in the time sequence reported by, e.g., [20, 29]. A nonlinear theory can be constructed using the present linear theory as a first-order approximation.

Further investigations are necessary to verify the present theoretical outcomes and to examine the nonlinear responses. For instance, if a very dense arrangement of force sensors along a flexible pipe model is technically possible, such an experiment may provide information to deepen our discussion. This study considered only the transverse component of VIV; however, the inline components have been reported to be indispensable for evaluating the fatigue damage to the riser, which could possibly be dealt with by extending the wake oscillator modeling.

4 Conclusion

This study has investigated the modal growth of the structural and lift force modes in a riser pipe vibrating owing to vortex-induced forces. A linear theory of the VIV occurring in the riser was built to understand the modal growth through an eigenvalue analysis. The following conclusions may be drawn:

- It is the fluid–structure interaction matrices that determine the intensity of interactions between the structural and lift force modes, as well as the interference among different frequency components.
- The presence of flow shear results in the excitation of higher structural modes than a uniform flow velocity profile. The excited structural modes are supplied energy by the same mode of the lift force and by higher modes of lift forces.
- The simplified interpretation using the rigid body approximates well the phase of the lift force mode relative to the structural mode that grows remarkably.
- The presence of flow shear grows multiple frequency components. The number of the components is closely related to the shear strength; a very strong shear results in a smaller number of growing frequency components than does a relatively weak shear.

Acknowledgements This study was financially supported by a Grant-in-Aid for Scientific Research (B) (no. 15H04211).

Appendix

In this appendix, we prove that the governing equation of lift force, Eq. (2), can be linearized under the assumption that the amplitude of VIV is very small. Let C_L and Y have the forms as follows:

$$\begin{cases} C_\mathrm{L} = \delta e^{\mathrm{i}\omega t} \\ Y = \delta C_\mathrm{Y} e^{\mathrm{i}\omega t} \end{cases},$$

respectively, where ω denotes the circular frequency, and δ denotes the amplitude, which is assumed to be very small. The amplitude of Y is the same order of δ as the amplitude of C_L; thus, $C_\mathrm{Y} = O(\delta^0) = O(1)$, where O is Landau notation. The magnitudes of the terms in Eq. (2) are evaluated in terms of the order of δ. Substituting those into the dimensionless form of Eq. (2):

$$C_\mathrm{L}'' - 2\xi\omega_\mathrm{v}\left(1 - \frac{P'}{f^2}C_\mathrm{L}^2\right)C_\mathrm{L}' + \omega_\mathrm{v}^2 C_\mathrm{L} = \frac{f}{k^*}Y'',$$

the magnitudes of the terms are evaluated as follows:

$$\underbrace{-\omega^2\delta}_{O(\delta)} - \left(\underbrace{1}_{O(0)} - \underbrace{\frac{P'}{f^2}\delta^2 e^{2\mathrm{i}\omega t}}_{O(\delta^2)}\right)\underbrace{2\mathrm{i}\xi\omega_\mathrm{v}\omega\delta}_{O(\delta)} + \underbrace{\omega_\mathrm{v}^2\delta}_{O(\delta)} = \underbrace{-\frac{f}{k^*}\omega^2 C_\mathrm{Y}\delta}_{O(\delta)}.$$

It follows that the terms of $O(\delta)$ become leading terms. Taking only the leading terms yields

$$-\omega^2\delta - 2\mathrm{i}\xi\omega_\mathrm{v}\omega\delta + \omega_\mathrm{v}^2\delta = -\frac{f}{k^*}\omega^2 C_\mathrm{Y}\delta,$$

which is equivalent to Eqs. (3) and (8).

References

1. Chaplin JR, Bearman PW, Huera-Huarte FJ, Pattenden RJ (2005) Laboratory measurements of vortex-induced vibrations of a vertical tension riser in a stepped current. J Fluids Struct 21(1):3–24
2. Trim AD, Braaten H, Lie H, Tognarelli MA (2005) Experimental investigation of vortex-induced vibration of long marine risers. J Fluids Struct 21(3):335–361
3. Rheem CK, Suzuki H, Kokubun K (2009) VIV response of inclined underwater line structure. J Jpn Soc Naval Arch Ocean Eng 9:97–105 (in Japanese)
4. Assi GRS, Srinil N, Freire CM, Korkischko I (2014) Experimental investigation of the flow-induced vibration of a curved cylinder in convex and concave configurations. J Fluids Struct 44:52–66
5. Franzini GR, Pesce CP, Gonçalves RT, Fujarra ALC, Mendes P (2016) Experimental investigations on vortex-induced vibrations with a long flexible cylinder. Part I: Modal-amplitude analysis with a vertical configuration In: Proceedings of the 11th international conference on flow-induced vibration (2016)
6. Franzini GR, Pesce CP, Gonçalves RT, Fujarra ALC, Mendes P (2016) Experimental investigations on vortex-induced vibrations with a long flexible cylinder. Part II: Effect of axial motion excitation in a vertical configuration In: Proceedings of the 11th international conference on flow-induced vibration (2016)
7. Rateiro F, Fujarra ALC, Pesce CP, Gonçalves RT, Franzini GR, Mendes P (2016) Experimental investigations on vortex-induced vibrations with a long flexible cylinder. Part III: Modal-amplitude analysis with a catenary configuration In: Proceedings of the 11th international conference on flow-induced vibration (2016)
8. Han Q, Ma Y, Xu W, Lu Y, Cheng A (2017) Dynamic characteristics of an inclined flexible cylinder undergoing vortex-induced vibrations. J Sound Vib 394:306–320
9. Baarholm GS, Larsen CM, Lie H (2006) On fatigue damage accumulation from in-line and cross-flow vortex-induced vibrations on risers. J Fluids Struct 22:109–127
10. Vandiver JK, Lee L (2003) SHEAR7 V4.3 Program theoretical manual

11. Larsen CM, Vikestad K, Yttervik R, Passano E (2000) VIVANA–theorey manual. MARINTEK Report MTF00-023
12. Suzuki H, Kimura R, Uto S, Rheem CK, Kokubun K, Arima Y (2008) Developmemt of time domain VIV response analysis method based on measured VIV hydrodynamic force. J Jpn Soc Naval Arch Ocean Eng 8:259–266 (in Japanese)
13. Tsukada RI, Morooka CK (2016) A numerical procedure to calculate the VIV response of a catenary riser. Ocean Eng 122:145–161
14. Evangelinos C, Lucor D, Karniadakis GE (2000) Dns-derived force distribution on flexible cylinders subject to vortex-induced vibraion. J Fluids Struct 14:429–440
15. Pan ZY, Cui WC, Miao QM (2007) Numerical simulation of vortex-induced vibration of a circular cylinder at low mass-damping using rans code. J Fluids Struct 23:23–37
16. Huang K, Chen HC, Chen CR (2011) Numerical scheme for riser motion calculation during 3-D VIV simulation. J Fluids Struct 27:947–961
17. Wang E, Xiao Q (2016) Numerical simulation of vortex-induced vibration of a vertical riser in uniform and linearly sheared currents. Ocean Eng 121:492–515
18. Sheinbaum J, Badan A, Ochoa J, Candela J, Rivas D, Gonzalez JI (2007) Full-water column current observations in the central Gulf of Mexico. Final report OCS Study MMS 2007-022
19. Vandiver JK, Allen D, Li L (1996) The occurrence of lock-in under highly sheared conditions. J Fluids Struct 10:555–561
20. Wl Chen, Zhang QQ, Li H, Hu H (2015) An experimental investigation on vortex induced vibration of a flexible inclined cable under a shear flow. J Fluids Struct 54:297–311
21. Nishi Y, Doan PV (2015) Distribution of damping device on riser pipe in sheared currents. Ocean Eng 104:489–499
22. Mathelin L, de Langre E (2005) Vortex-induced vibrations and waves under shear flow with a wake oscillator model Euro. J Mech B Fluids 24:478–490
23. Pesce CP, de Martins CA, Silveira LMY (2006) J Offshore Mech Arctic Eng. Riser-soil interaction: local dynamics at TDP and a discussion on the eigenvalue and the VIV problems 128:39–55
24. Violette R, de Langre E, Szydlowski J (2010) A linear stability approach to vortex-induced vibrations and waves. J Fluids Struct 26:442–466
25. Cheng Y, Vandiver JK, Moe G (2002) The linear vibration analysis of marine risers using the WKB-based dynamic stiffness method. J Sound Vib 251(4):750–760
26. Sparks CP (2007) Fundamental of marine riser mechanics: basic principles and simplified analyses. PennWell, Tulsa
27. Chatjigeorgiou IK (2008) Application of the WKB method to catenary-shaped slender structure. Math Comp Modell 48:249–257
28. Violette R, de Langre E, Szydlowski J (2007) Computation of vortex-induced-vibrations of long structures using a wake oscillator model: comparison with DNS and experiments. Comp Struct 85:1134–1141
29. Srinil N (2011) Analysis and prediction of vortex-induced vibrations of variable-tension vertical risers in linearly sheared currents. App Ocean Res 33:41–53
30. Srinil N, Zanganeh H (2012) Modelling of coupled cross-flow/in-line vortex-induced vibrations using double Duffing and Van der Pol oscillators. Ocean Eng 53:83–97
31. Tamura Y, Matsui G (1979) Wake-oscillator model of vortex-induced oscillation of circular cylinder In: Proceedings of the 5th international conference on wind engineering, pp 1085–1094
32. Doan VP, Nishi Y (2015) Modeling of fluid-structure interaction for simulating vortex-induced vibration of flexible riser: finite difference method combined with wake oscillator model. J Mar Sci Tech 20(2):309–321
33. Nishi Y, Kokubun K, Hoshino K, Uto S (2009) Quasisteady theory for the hydrodynamic forces on a circular cylinder undergoing vortex-induced vibration. J Mar Sci Tech 14(3):285–295
34. Strang G (2016) Introduction to linear algebra, 5th edn. Wellesley Cambridge Press, Wellesley
35. McKone KP, Walker ND, Weeks E (2007) Full-water column currents near the sigsbee escarpment (91–92 deg. w. longitude) and relationships with the loop current and associated warm- and cold-core eddies OCS Study. MMS 2007-056
36. Welsh SE, Inoue M, Rouse LJ Jr, Weeks E (2009) Observation of the deepwater manifestation of the loop current and loop current rings in the eastern Gulf of Mexico OCS Study MMS 2009-050
37. Fratantoni DM, Gellers A, Sharma N (2014) On the oceanography of Brazil's equatorial margin: hazardous offshore currents and strategies for mitigation In: Proceedings of Rio Oil and Gas Expo and Conferece 2014 (2014)
38. Song JN, Lu L, Teng B, Park HI, Tang GQ, Wu H (2011) Laboratory tests of vortex-induced vibrations of a long flexible riser pipe subjected to uniform flow. Ocean Eng 38:1308–1322
39. Lie H, Kaasen KE (2006) Modal analysis of measurements from a large-scale VIV model test of a riser in linearly sheared flow. J Fluids Struct 22:557–575
40. Yamagata T (1985), Stability of a simple air–sea coupled model in the tropics. coupled ocean-atmosphere models. In: Nihoul CJ (ed) Elsevier Oceanogr Ser. Elsevier, pp 637–657
41. Ohshima KI, Nihashi S (2005) A simplified ice–ocean coupled model for the Antarctic ice melt season. J Phys Oceanogr 35:188–201
42. Tsuta T, Bai J, Hanano T (1996) High-speed stability and dynamic response analysis of motorcycle-driver system. Trans Jpn Soc Mech Eng Ser C 62(593):76–82 (in Japanese)
43. Arisaka T, Ono K, Sato H (1994) Analytical study of stability of strip-roll coupling system in cold rolling. Trans Jpn Soc Mech Eng Ser C 60(570):91–97 (in Japanese)